Ceramics International 46 (2020) 331–342

Contents lists available at ScienceDirect

Ceramics International

journal homepage: www.elsevier.com/locate/ceramint

Stress analysis of the thermal barrier coating system near a cooling hole considering the free-edge effect

Jishen Jiang, Xianfeng Ma*, Biao Wang

Sino-French Institute of Nuclear Engineering and Technology, Sun Yat-Sen University, Zhuhai, 519082, Guangdong, China

ARTICLE INFO

Keywords:
Thermal barrier coating
Film cooling
Edge-effect
Peeling moment
Shear force

ABSTRACT

Due to the thermal mismatch between layers and the free-edge effect, interfacial peeling and shear stresses are generated locally around the edges of cooling holes in a thermal barrier coating (TBC)–film cooling system. These interfacial peeling and shear stresses may lead to modes I and II edge delamination, resulting in TBC spallation around the cooling hole. In this study, analytical and numerical models were built to study the stress and interfacial cracking behaviors of TBCs near the cooling hole. Analytical solutions for interfacial peeling moment and shear force at each layer were obtained to analyze the free-edge effect on the stress distributions in TBCs, and they were verified by the finite element calculations. The results showed that interfacial peeling moment and shear force were functions of the hole radius and thicknesses of top coat and oxide layer. The increase of interfacial peeling moment and shear force raised the likelihood of edge cracking around the hole. Derived by the local stresses, the interfacial cracks in TBCs initiated and propagated from the hole edge upon cooling.

1. Introduction

Although thermal barrier coatings (TBCs) have been applied in high temperature components of gas turbines as thermal protection techniques for decades, the premature failure greatly shortens their service lifetimes [1]. The complex multilayered structure leads to huge thermal stresses in the TBC system during thermal cycling, resulting in dramatic interfacial delamination [2]. The stress behavior in TBCs could be more complicated around the cooling hole in the TBC-film cooling system under operating conditions. The steep temperature gradient associated with the mix of hot and coolant gases and the geometry constraint make the cooling hole to be another major source of TBC failure [3–6]. The effect of three-dimensional temperature gradient on the stress evolution of TBCs near the cooling hole has been numerically studied in our previous research [4]. However, some researches pointed out that even regardless of the spatial temperature gradient, the cooling hole could still be regarded as a stress concentrator to derive TBC cracks [7,8]. Due to the free-edge effect, the interfacial peeling stresses (normal to the interface) and shear stresses could be locally generated around the cooling hole, which may aggravate the local stress state and even promote interfacial crack initiation of TBCs. Therefore, investigation of the stress field and stress-induced interfacial cracking behavior of TBCs adjacent to the cooling hole is required to evaluate the reliability and durability of TBCs.

A TBC system typically consists of four layers: the ceramic top coat (TC), the thermally grown oxide (TGO), the metallic bond coat (BC), and the underlying superalloy substrate. Upon cooling, large residual stresses are generated by thermal mismatches in the multilayered TBC system [9]. To this end, Hsueh [10] and Zhang et al. [11] established analytical solutions to calculate the residual stresses in the multilayered TBCs. These solutions were generally based on the classic beam bending theory and were exact for positions far from the free edges. However, at the free edges of the thin plate/disk, the in-plane residual stresses could be converted to peeling (normal to the interface) and shear stresses at the interface because of the free-edge effect. This phenomenon is difficult to describe with the above-mentioned solutions [12]. Thus, considerable efforts have been devoted to identification of analytical solutions for the interfacial peeling and shear stresses in multilayered systems [13–16]. However, the exact closed-form solutions for the distributions of the peeling and shear stresses were quite difficult to derive, and only some approximate solutions were obtained. It is worth noting that Moore [17] and Hsueh [18] found that the interfacial peeling moment and shear force were also able to characterize mode I and mode II edge cracking. The peeling moment and shear force are derived from the localized peeling and shear stresses, respectively, and solutions for them were relatively easy to obtain. In Hsueh's solutions

* Corresponding author.
E-mail address: maxf6@mail.sysu.edu.cn (X. Ma).

https://doi.org/10.1016/j.ceramint.2019.08.267
Received 16 July 2019; Received in revised form 23 August 2019; Accepted 27 August 2019
Available online 28 August 2019

[10,18], only three constant unknown parameters (i.e., the uniform strain component c, the position of the bending axis t_b, and the curvature $1/\rho$) required solution, and only three boundary conditions needed to be satisfied. The solutions were exact for the outside free edges of multilayered structures, but they may not be suitable for the free edges of the cooling hole. In the model of a thin plate/disk with a hole, these three parameters (i.e., c, t_b, and $1/\rho$) are functions of the radii of the disk and hole instead of constants, and the boundary conditions differ from those without holes. Therefore, equations for the three parameters should be reconstructed, and the analytical solutions for the interfacial peeling moment and shear force at the free edges of the cooling hole in a TBC system must be improved. Furthermore, derived by the complex local stresses around the hole, interfacial crack may initiate and propagated from the hole edge, thus a reliable model to predict the interfacial cracking behavior of TBCs is highly desirable.

This study was performed to investigate the stress distributions and stress-induced interfacial cracks at the edges of the cooling hole in a TBC system under a uniform temperature change. To this end, a model of an infinite elastic multilayered disk with a round center hole was constructed without consideration of peeling at the outside edges. Analytical solutions for the interfacial peeling moment and shear force at each interface were established based on the mechanics of elasticity and the thin plate bending theory. Furthermore, the stress distributions in double- and four-layered coating systems were analyzed by the analytical solutions and finite-element (FE) calculations. The effects of the hole radius and thicknesses of TGO and TC layers on the interfacial peeling moment and shear forces were further investigated. Finally, stress-induced interfacial cracking behaviors in TBCs near the cooling hole were numerically studied by the cohesive zone model (CZM).

2. Theoretical formulation

2.1. Problem description

Fig. 1a presents a model of an infinite elastic TBC-substrate thin disk with a round cooling hole. The disk undergoes uniform temperature loading without other external loadings. Considering the symmetric geometry and thermal loading, the three-dimensional model is simplified into a two-dimensional axisymmetric model (Fig. 1b). The thermal mismatch under temperature change leads to in-plane tensile/compressive stresses in each layer and thus bending of the system. As illustrated in Fig. 1c, near the edges of the hole, the free-edge effect leads to interfacial peeling and shear stresses that are represented by the peeling moment, M_p, and the shear force, V, per unit circumferential length, respectively. For analytical solutions, thermal stresses are first calculated based on the thin plate bending theory, and M_p and V are then calculated with the equilibrium equations of moment and force.

Fig. 2 shows a sketch of the two-dimensional axisymmetric multilayered disk model for analytical calculation. The n layers of coating with individual thicknesses of h_i are bonded sequentially to the substrate with a thickness of h_s, so the total thickness of the disk h_{total} is calculated by

$$h_{total} = h_s + \sum_{i=1}^{n} h_i \tag{1}$$

The subscript i represents the number of layers of the coating, ranging from 1 to n, and layer 1 represents the layer in direct contact with the substrate. In addition, the interfaces between the layers are also sequentially numbered by $k = 1$ to n, and interface 1 lies between layer 1 and the substrate. A straight hole with a radius of a is located in the center of the disk with a radius of b. Note that $b \gg a$ and $b \gg h_{total}$, and the outside edge (right edge) of the disk is allowed to deform in the radial direction but must remain in-plane and vertical. These settings allow the assumption that the disk is infinite. A cylindrical coordinate system is defined to parameterize positions within the disk such that the z-axis is collinear with the center line of the hole and the r-axis is collinear with interface 1. Hence, interface k ($k = i+1$) between layers i and $i+1$ is located at $z = t_i$, and the free surfaces of the coating and substrate are located at $z = t_n$ and $z = -t_s$, respectively. Based on these definitions, the relationship between h_i and t_i can be expressed as

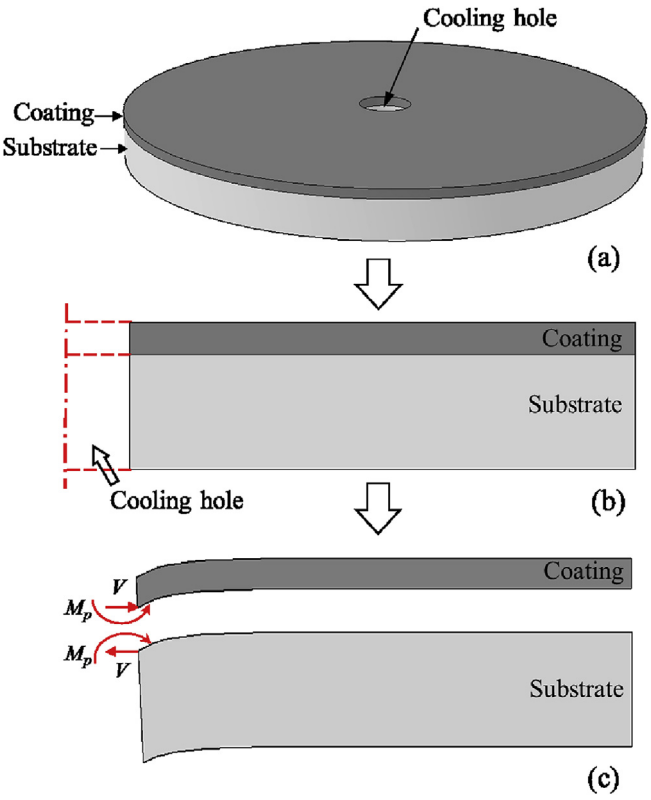

Fig. 1. Models of a coating-substrate system with a cooling hole: (a) three-dimensional model; (b) two-dimensional axisymmetric model; (c) sketch of interfacial peeling moment M_p and shear force V after cooling to room temperature.

$$t_i = \sum_{j=1}^{i} h_j \ (i = 1 \ \ to \ n) \tag{2}$$

2.2. Governing equations

The thin plate bending theory is used to obtain closed-form solutions for thermal stress in the region remote from the free edges. The disk is assumed to be thin, such that h_{total}/b is less than 0.2, and the deflection of the disk is assumed to be small. Under uniform temperature change ΔT, all layers of the disk will expand (upon heating) or shrink (upon cooling) and then bend due to the thermal mismatch. Based on the study by Hsueh and Evans [19], the radial strain of the multilayered disk, ε_{rr}, can be decomposed into a bending component, ε_b, and a uniform strain component, c, such that

$$\varepsilon_{rr} = \varepsilon_b + c = \frac{z - t_b}{\rho} + c \tag{3}$$

where ρ is the radius of the curvature and $z = t_b$ is the location of the bending axis, where the bending strain component is zero (Fig. 2). Because its solution is difficult to obtain directly, the curvature, $\frac{1}{\rho}$, is expressed as the function of the deflection, w, of the disk based on the bending theory, namely

$$\frac{1}{\rho} = -\frac{d^2w}{dr^2} \tag{4}$$

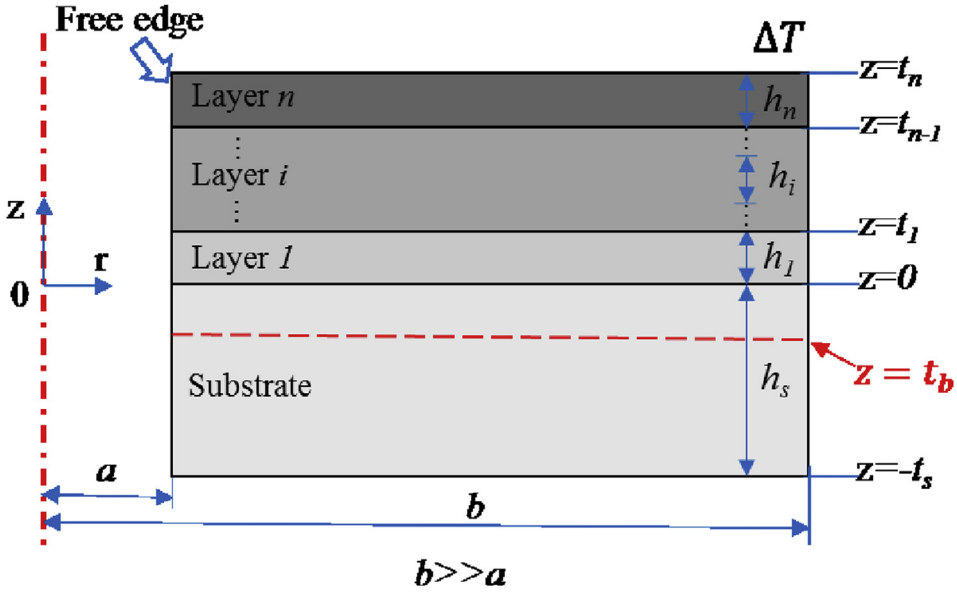

Fig. 2. A two-dimensional axisymmetric multilayered model for analytical calculation.

By substituting Eq. (4) into Eq. (3),

$$\varepsilon_{rr} = -(z - t_b)\frac{d^2w}{dr^2} + c \tag{5}$$

Similarly, the hoop strain, $\varepsilon_{\theta\theta}$, can be expressed as

$$\varepsilon_{\theta\theta} = -\frac{z - t_b}{r}\frac{dw}{dr} + c \tag{6}$$

For all layers, the stress-strain constitutive equations are

$$\varepsilon_{rr} = \frac{1}{E}[\sigma_{rr} - v(\sigma_{\theta\theta} + \sigma_{zz})] + \alpha\Delta T \tag{7a}$$

$$\varepsilon_{\theta\theta} = \frac{1}{E}[\sigma_{\theta\theta} - v(\sigma_{rr} + \sigma_{zz})] + \alpha\Delta T \tag{7b}$$

where E is the elastic modulus, α is the thermal expansion coefficient, and σ_{rr}, $\sigma_{\theta\theta}$, and σ_{zz} are the stress components in the r, θ, and z directions, respectively. In the thin plate bending theory, the stress component, σ_{zz}, is negligibly small. Thus, combining Eqs. (5)–(7), the stress components are expressed as

$$\sigma_{rr} = \frac{-E(z - t_b)}{1 - v^2}\left(\frac{d^2w}{dr^2} + \frac{v}{r}\frac{dw}{dr}\right) + \frac{Ec - E\alpha\Delta T}{1 - v} \tag{8a}$$

$$\sigma_{\theta\theta} = \frac{-E(z - t_b)}{1 - v^2}\left(\frac{1}{r}\frac{dw}{dr} + v\frac{d^2w}{dr^2}\right) + \frac{Ec - E\alpha\Delta T}{1 - v} \tag{8b}$$

The equations for the in-plane stress distribution are suitable for all layers of the disk, and only three unknown parameters, i.e., c, t_b and w, must be solved.

The parameters c and t_b are calculated from the following boundary conditions. First, the resultant force derived from the uniform strain component is zero, such that

$$\frac{E_s}{1 - v_s}(c - \alpha_s\Delta T)h_s + \sum_{i=1}^{n}\frac{E_i}{1 - v_i}(c - \alpha_i\Delta T)h_i = 0 \tag{9}$$

thus,

$$c = \frac{\frac{E_s h_s \alpha_s \Delta T}{1 - v_s} + \sum_{i=1}^{n}\frac{E_i h_i \alpha_i \Delta T}{1 - v_i}}{\frac{E_s h_s}{1 - v_s} + \sum_{i=1}^{n}\frac{E_i h_i}{1 - v_i}} \tag{10}$$

Eq. (10) indicates that the uniform strain component c is irrelevant to the radii of the disk and the hole (i.e., c = constant). Second, the resultant force derived from the bending strain component is zero, such that

$$\int_{-t_s}^{0}\frac{-E_s(z - t_b)}{1 - v_s^2}\left(\frac{d^2w}{dr^2} + \frac{v_s}{r}\frac{dw}{dr}\right) dz + \sum_{i=1}^{n}\int_{t_{i-1}}^{t_i}\frac{-E_i(z - t_b)}{1 - v_i^2}\left(\frac{d^2w}{dr^2} + \frac{v_i}{r}\frac{dw}{dr}\right)dz = 0 \tag{11}$$

where t_{i-1} (namely t_0) is defined as zero when $i = 1$. Thus, t_b can be determined as a function of w.

The above-mentioned variables, such as the strain/stress components and t_b, are functions of w. Based on the bending theory, the differential equation for the symmetrical bending of a thin disk under only uniform thermal loading can be expressed as [20].

$$\frac{d}{dr}\left[\frac{1}{r}\frac{d}{dr}\left(r\frac{dw}{dr}\right)\right] = 0 \tag{12}$$

For the case of a disk with a circular hole at the center, the general solution for w is

$$w = c_1 r^2 + c_2 ln(r/b) + c_3 \tag{13a}$$

with

$$\frac{dw}{dr} = 2c_1 r + \frac{c_2}{r} \tag{13b}$$

$$\frac{d^2w}{dr^2} = 2c_1 - \frac{c_2}{r^2} \tag{13c}$$

where b is the radius of the disk and c_1, c_2, and c_3 are constants of integration that can be determined from the following boundary conditions:

i) At the hole edge, the resultant radial bending moment per unit circumferential length, M_r, is zero, such that

$$M_r = 0, \ when \ r = a \tag{14}$$

For the multilayered disk, M_r is defined as

$$M_r = \int_{-t_s}^{t_n}\sigma_{rr}(z - t_b)dz = \int_{-t_s}^{0}\sigma_{rr}^{s}(z - t_b)dz + \sum_{i=1}^{n}\int_{t_{i-1}}^{t_i}\sigma_{rr}^{i}(z - t_b)dz \tag{15}$$

with

$$\sigma_{rr}^{s} = \frac{-E_s(z - t_b)}{1 - v_s^2}\left(\frac{d^2w}{dr^2} + \frac{v}{r}\frac{dw}{dr}\right) + \frac{E_s c - E_s\alpha_s\Delta T}{1 - v_s} \tag{16a}$$

$$\sigma_{rr}^{i} = \frac{-E_i(z-t_b)}{1-v_i^2}\left(\frac{d^2w}{dr^2} + \frac{v}{r}\frac{dw}{dr}\right) + \frac{E_i c - E_i\alpha_i\Delta T}{1-v_i} \tag{16b}$$

where the superscripts s and i denote the substrate s and layer i of the coating, respectively. Substituting Eqs. (15) and (16) into Eq. (14), we obtain

$$\begin{aligned}&\frac{E_s h_s^2}{1-v_s}\left(\frac{h_s}{3} + \frac{t_b^{r=a}}{2}\right)\left(-2c_1 + \frac{1-v_s}{1+v_s}\frac{c_2}{a^2}\right)\\ &+ \sum_{i=1}^{n}\frac{E_i h_i}{1-v_i}\left[\left(t_{i-1}^2 + t_{i-1}h_i + \frac{h_i}{3}\right) - t_b^{r=a}\left(t_{i-1} + \frac{h_i}{2}\right)\right]\left(-2c_1 + \frac{i-v_i}{1+v_i}\frac{c_2}{a^2}\right)\\ &= \frac{E_s h_s(c-\alpha_s\Delta T)}{1-v_s}\left(\frac{h_s}{2} + t_b^{r=a}\right)\\ &\quad - \sum_{i=1}^{n}\frac{E_i h_i(c-\alpha_i\Delta T)}{1-v_i}\left(t_{i-1} + \frac{h_i}{2} - t_b^{r=a}\right)\end{aligned} \tag{17}$$

ii) According to the assumptions mentioned above, the outside edge of the disk is allowed to move radially but must remain in-plane and vertical, which means that the deflection w is constant and that dw/dr is zero. For simplification, w is assumed to be zero. As a result,

$$w = 0,\ and\ \frac{dw}{dr} = 0,\ when\ r = b \tag{18}$$

from which

$$c_1 b^2 + c_3 = 0 \tag{19}$$

and

$$2c_1 b^2 + c_2 = 0 \tag{20}$$

Substituting Eqs. (13) and (20) into Eq. (11), the location of the bending axis, t_b, is expressed as the function of r

$$t_b = \frac{\frac{-E_s h_s^2}{1-v_s}\left(1 + \frac{1-v_s}{1+v_s}\frac{b^2}{r^2}\right) + \sum_{i=1}^{n}\frac{E_i h_i(2t_{i-1}+h_i)}{1-v_i}\left(1 + \frac{1-v_i}{1+v_i}\frac{b^2}{r^2}\right)}{\frac{2E_s h_s}{1-v_s}\left(1 + \frac{1-v_s}{1+v_s}\frac{b^2}{r^2}\right) + \sum_{i=1}^{n}\frac{2E_i h_i}{1-v_i}\left(1 + \frac{1-v_i}{1+v_i}\frac{b^2}{r^2}\right)} \tag{21}$$

Combining Eqs. (17), (19) and (20), we obtain

$$\begin{aligned}c_1 = &\frac{-\frac{E_s h_s(c-\alpha_s\Delta T)}{1-v_s}\left(\frac{h_s}{2} + t_b^{r=a}\right) + \sum_{i=1}^{n}\frac{E_i h_i(c-\alpha_i\Delta T)}{1-v_i}\left(t_{i-1} + \frac{h_i}{2} - t_b^{r=a}\right)}{\frac{2E_s h_s^2}{1-v_s}\left(\frac{h_s}{3} + \frac{t_b^{r=a}}{2}\right)\left(1 + \frac{1-v_s}{1+v_s}\frac{b^2}{a^2}\right)}\\ &+ \sum_{i=1}^{n}\frac{2E_i h_i}{1-v_i}\left[\left(t_{i-1}^2 + t_{i-1}h_i + \frac{h_i^2}{3}\right) - t_b^{r=a}\left(t_{i-1} + \frac{h_i}{2}\right)\right]\\ &\left(1 + \frac{1-v_i}{1+v_i}\frac{b^2}{a^2}\right)\end{aligned} \tag{22}$$

Combining Eqs. (13a), (19) and (20), and (22), the deflection w can be calculated by

$$w = c_1\left[r^2 - 2b^2 ln\left(\frac{r}{b}\right) - b^2\right] \tag{23}$$

By now, the general solutions for the stress/strain distributions in all layers of the disk are complete. The stresses both in layers of coating and substrate are functions of r and z. The above solutions are exact for positions remote from the free edges.

2.3. Interfacial peeling moments M_p and shear forces V

Around the free edges of the hole, the in-plane thermal stresses are converted to peeling stress, σ_{zz}, and shear stress, τ_{rz}, at the interface. Since exact solutions for the distributions of σ_{zz} and τ_{rz} are quite difficult to derive, the interfacial peeling moment and shear force derived from the localized σ_{zz} and τ_{rz} are chosen to characterize mode I and mode II edge cracking [17,18]. At interface$k$ ($1 \le k \le n$), the peeling moment, $\hat{M}_p^k$, induced by the peeling stress, σ_{zz}^k, is expressed as

$$\hat{M}_p^k = \int_0^{2\pi}\int_a^b \sigma_{zz}^k(r-a)\cdot r dr d\theta = \int_a^b \sigma_{zz}^k(r-a)\cdot 2\pi r dr \tag{24}$$

and the shearing force, $\hat{V}^k$, induced by the shear stress, τ_{rz}^k, is expressed as

$$\hat{V}^k = \int_0^{2\pi}\int_a^b \tau_{rz}^k\cdot r dr d\theta = \int_a^b \tau_{rz}^k\cdot 2\pi r dr \tag{25}$$

Therefore, the peeling moment, M_p^k, and the shear force, V^k, per unit circumferential length in the region of the hole edge are calculated by

$$M_p^k = \frac{\hat{M}_p^k}{2\pi a} = \frac{1}{a}\int_a^b \sigma_{zz}^k(r-a) r dr \tag{26}$$

and

$$V^k = \frac{\hat{V}^k}{2\pi a} = \frac{1}{a}\int_a^b \tau_{rz}^k r dr \tag{27}$$

Since exact solutions for σ_{zz}^k and τ_{rz}^k are hardly to obtain, the interfacial peeling moments and shear forces at the hole edge can be calculated by σ_{rr} according to a superposition procedure [18,21]. The free-surface condition at the hole can be determined by the following two steps: first, the stresses of σ_{rr}^s and σ_{rr}^i (exactly calculated in Subsection 2.2) are assumed to be distributed throughout the system; second, imaginary tractions equal and opposite to the stresses at $r = a$ (i.e., $-\sigma_{rr}^{s,r=a}$ and $-\sigma_{rr}^{i,r=a}$) are applied at the corresponding locations along the hole edges. In this way, a stress-free state is achieved at the hole edges, and the stress in regions far from the hole remains unchangeable due to Saint-Venant's principle. The stress field near the hole area is the superposition of fields of σ_{rr}^s and σ_{rr}^i and a field induced by the imaginary tractions, and only the latter leads to interfacial peeling and shear stresses. Therefore, $\hat{M}_p^k$ and $\hat{V}^k$ are equivalent to the peeling moment and the shear force, respectively, derived from the imaginary tractions applied above interface k, namely

$$\hat{M}_p^k = -\sum_{i=k}^{n}\int_{t_{i-1}}^{t_i}\sigma_{rr}^{i,r=a}(z - t_{k-1})\cdot 2\pi a dz \tag{28}$$

and

$$\hat{V}^k = -\sum_{i=k}^{n}\int_{t_{i-1}}^{t_i}\sigma_{rr}^{i,r=a}\cdot 2\pi a dz \tag{29}$$

Thus, M_p^k, and V^k are calculated by

$$M_p^k = -\sum_{i=k}^{n}\int_{t_{i-1}}^{t_i}\sigma_{rr}^{i,r=a}(z - t_{k-1}) dz \tag{30}$$

and

$$V^k = -\sum_{i=k}^{n}\int_{t_{i-1}}^{t_i}\sigma_{rr}^{i,r=a} dz \tag{31}$$

Substituting Eqs. (13), (16) and (20) into Eqs. (30) and (31), we obtain

$$\begin{aligned}M_p^k = &-\sum_{i=k}^{n}\frac{2E_i h_i}{1-v_i}\left[-\left(t_{i-1}^2 + t_{i-1}h_i + \frac{h_i^2}{3}\right) + (t_{k-1} + t_b^{r=a})\left(t_{i-1} + \frac{h_i}{2}\right)\right.\\ &\left. - t_b^{r=a}t_{k-1}\right]\left(1 + \frac{1-v_i}{1+v_i}\frac{b^2}{a^2}\right)c_1\\ &- \sum_{i=k}^{n}\frac{E_i h_i}{1-v_i}(c-\alpha_i\Delta T)\left(t_{i-1} - t_{k-1} + \frac{h_i}{2}\right)\end{aligned} \tag{32}$$

and

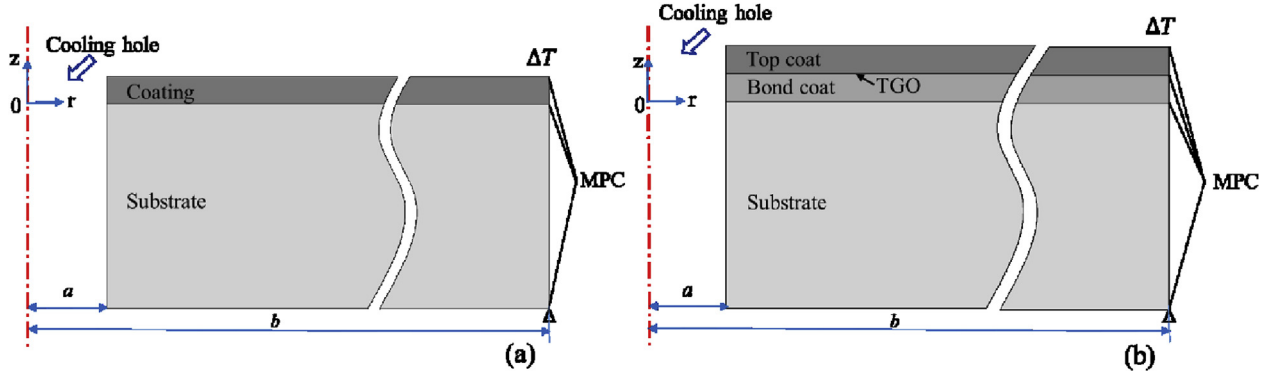

Fig. 3. Geometries of FE models with boundary conditions: (a) double-layered model; (b) four-layered model.

$$V^k = -\sum_{i=k}^{n} \frac{E_i h_i}{1-\nu_i}\left[-2c_1\left(t_{i-1}+\frac{h_i}{2}-t_b^{r=a}\right)\left(1+\frac{1-\nu_i}{1+\nu_i}\frac{b^2}{a^2}\right)+c-\alpha_i\Delta T\right] \tag{33}$$

where c, $t_b^{r=a}$, and c_1 are given by Eqs. (10), (21) and (22), respectively. The solutions for the interfacial peeling moment and shear force at each interface are now complete and are independent of the number of coating layers.

3. Numerical modeling

Numerical models are built in ABAQUS to i) confirm the accuracy of the analytical solutions and ii) study the stress field and interfacial cracking behavior of TBCs near the cooling hole. To this end, two two-dimensional axisymmetric FE models of double- and four-layered coating-substrate systems with cooling holes are constructed as examples, and their geometries and boundary conditions are illustrated schematically in Fig. 3. The double-layered model in Fig. 3a consists of a ceramic coating (i.e., the TC) layer and a super-alloy substrate layer, and the four-layered model in Fig. 3b consists of a TC layer, a TGO layer, a BC layer, and a substrate layer. All of the layers are well-bonded together. The radius of the hole, a, was varied from 0.1 to 3 mm to study the influence of the cooling hole's geometry on the edge delamination. The radius of the model, b, is set as 25 mm to maintain $b \gg a$ and $b \gg h_{total}$. Multiple FE calculations prove that the results of stress fields, peeling moments, and shear forces around the hole are nearly unchanged for $b > 25$ mm.

The models undergo uniform cooling-down periods from stress-free states at high temperatures to room temperature (i.e., ΔT = -1200 °C) in 20 min. The outside edges of the models are restricted by the multipoint constraint (MPC) method so that they are allowed to move radially but must remain in-plane and vertical. The bottoms of the outside edges are restricted to move in the z direction to ensure that their deflections are zero. The top and bottom edges of the models and the edges of the holes are free from any constraints. The eight-node axisymmetric thermally coupled quadrilateral elements (CAX8T) are generated for FE meshing. The meshes in regions adjacent to the hole and all interfaces are refined to obtain sufficient accurate results, and the minimum mesh sized reaches 0.01 μm.

All layers are treated as elastic materials, and their material properties and thicknesses are listed in Table 1. Because the TGO layer can grow during application, its thickness is set to range from 0.001 to 0.01 mm to examine its influence on edge delamination. In addition, because a thicker TC layer brings about higher thermal insulation properties but a more severe thermal mismatch, the thickness of the TC layer is also set to vary from 0.05 to 0.3 mm. Unless otherwise noted, the thicknesses of the TGO and TC layers are set as 0.005 mm and 0.2 mm, respectively, for these calculations.

When the simulated distributions of interfacial peeling and shear stresses, $\sigma_{zz,k}$ and $\tau_{rz,k}$, are achieved, $\hat{M}_{p,k}$ and $\hat{V}_k$ can be respectively calculated by Eqs. (24) and (25), and $M_{p,k}$ and V_k can be respectively calculated by Eqs. (26) and (27). The FE results are then compared with the analytical results calculated by Eq. (28)~(33).

Table 1
Material properties and thicknesses of the thermal barrier coating–substrate system for finite element (FE) calculation.

Materials	E (GPa)	ν	α (× 10^{-6}/°C)	h (mm)
TC	20	0.1	10	0.05–0.3
TGO	400	0.2	8	0.001–0.01
BC	150	0.3	15	0.2
Substrate	200	0.25	18	1.5

Finally, to simulate the interfacial cracking behaviors in four-layered TBCs during the cooling period, the four-node axisymmetric cohesive zone elements (COHAX4) in nearly zero thicknesses are located at the TC/TGO/BC interfaces. Since the BC/substrate interface generally has good bonding performance, the interfacial crack between the BC and substrate is not considered. The interfacial cohesive zone model (CZM) in the FE calculation is characterized by a bilinear traction-separation law (TSL). It is assumed that the interface in the cohesive zone before crack tip has a linear elastic behavior before damage, and once the initiation criterion is satisfied, damage begins to initiate. Under continuous loadings, the damage accumulates until final failure occurs. Detailed description of CZM and their constitutive equations can be found in our previous research [22]. Under mixed-mode thermal loadings, a maximum minimal stress criterion is chosen for damage initiation, which can be expressed as [23].

$$max\left\{\frac{\langle\sigma_n\rangle}{\sigma_n^0}, \frac{\sigma_s}{\sigma_s^0}\right\} = 1 \tag{34}$$

where $\langle\cdot\rangle$ is the Macaulay bracket representing that damage cannot initiate under pure compressive stress, and σ_n^0 and σ_s^0 are the critical stresses in normal and shear directions, respectively. In the FE models, the TC/TGO and TGO/BC interfaces are assumed to have same interfacial properties. The acquired interfacial fracture parameters are listed as follows: the initial stiffness K = 200 GPa, the mode I and model II critical energy release rates (fracture toughness) $G_n^c = G_s^c$ = 20 J/m^2, and the critical stresses $\sigma_n^0 = \sigma_s^0$ = 200 MPa [22].

4. Results and discussion

4.1. Double-layered system

The analytical solutions for the double-layered system can be obtained by degenerating the relevant solutions presented in Sections 2.2 and 2.3. Detailed solutions are displayed in Appendix A. Fig. 4 shows the results of the deflection w and curvature $\frac{1}{\rho}$ along the r direction with a hole radius a of 1.5 mm. The analytical solution for w agrees well with

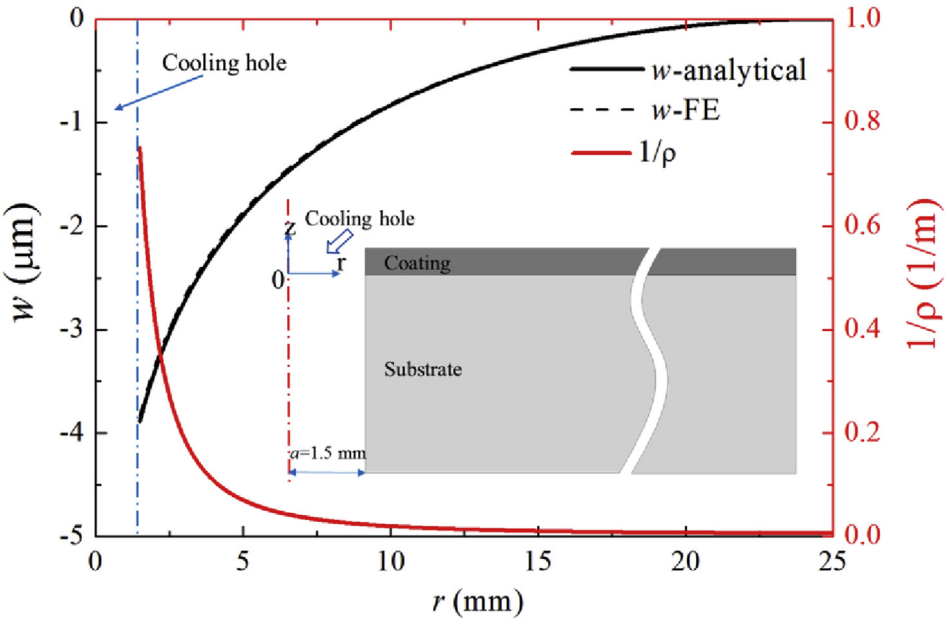

Fig. 4. Results of the deflection w and curvature $1/\rho$ of the disk along the radial direction.

the FE solution. Clearly, the curvature is the function of r, which differs from Hsueh's solution [10] for the system without a hole that the curvature keeps as a constant. The curvature reaches 0.75 m at the hole edge and sharply decreases along the radial direction to zero for $r = b$. This tendency can be explained by Eqs. (A. 5) through (A. 7). The increase of curvature near the hole will lead to high local strain and stress based on Eq. (3). Because excellent agreement was obtained between the analytical and FE solutions for deformations, the stress/strain fields remote from the hole edges calculated by analytical formulas also agree with the FE calculations.

Fig. 5 shows the FE results of the stress component distributions in the regions around the interface and hole edge. Due to thermal mismatching, the radial stress σ_{rr} is in a compressive state for the coating layer and in a tensile state for the substrate layer. The magnitude of σ_{rr} decreases near the free-edge of the hole (see Fig. 5a). Both the stress normal to the interface, σ_{zz}, and the shear stress, τ_{rz}, are zero in regions far from the hole edge. In the hole edge region, interfacial peeling and shear stresses (i.e., σ_{zz} and τ_{rz}) are induced by the thermal mismatch and free-edge effect.

Attention is now focused on the stress distribution along the interface. Fig. 6 shows the distributions of interfacial peeling and shear stresses, σ_{zz} and τ_{rz}, along the radial direction for various radii of the hole. Both σ_{zz} and τ_{rz} are found to be concentrated near the hole edge and then decay to negligible values in positions far from the hole ($r > \sim 1.0$ mm for σ_{zz} and $r > \sim 1.2$ mm for τ_{rz}). Near the hole region, σ_{zz} always changes sign from negative to positive. Because no external loadings are applied normal to the interface, the resultant force derived from the compressive peeling stresses is equivalent to that from the tensile peeling stresses. In the FE results, σ_{zz} and τ_{rz} are affected by the hole radius, especially for lower values of a. Although the tendencies for both σ_{zz} and τ_{rz} remain consistent, their magnitudes increase as the hole radius increases. However, when the radius of the hole is sufficiently large (for instance $a > 1.5$ mm), the stresses can hardly continue to increase, which indicates that they are nearly independent of the hole radius. Both σ_{zz} and τ_{rz} reach their minimum values (i.e., the maximum magnitudes) at the hole edge, and both $\sigma_{zz,min}$ and $\tau_{rz,min}$ decrease as the hole radius increases. It worth noting that the stresses at the hole edge may be subject to errors because of the free-edge stress singularity problem [24]. The resultant force induced by interfacial peeling stress should be as close to zero as possible, and mesh refinement near the hole edge is required to minimize the errors.

Fig. 7 displays the results of the interfacial peeling moments and shear forces induced by σ_{zz} and τ_{rz} for various hole radii. The analytical and FE results show excellent agreement for a hole with a large radius ($a > 1.5$ mm); however, differences appear for those with a small radius. Both peeling moments $\hat{M}_p$ and shear forces $\hat{V}$ increase almost linearly as the hole radius increases in the analytical and FE solutions. The analytical solutions are slightly larger than the analytical solutions for smaller holes. For the peeling moments M_p and shear forces V per unit circumferential length, the analytical results remain constant as the hole radius increases. This can be explained by Eqs. (A. 11) through (A. 13) that M_p and V are not functions of a and b. During the cooling-down period, M_p reaches 4 N and V reaches 40 N/mm at the interface. In the FE results, M_p and V both have positive correlations with the hole radius for smaller values of a; however, they also remain constant when a is greater than 1.5 mm.

In Fig. 7, a smaller hole radius leads to a larger difference between the analytical and FE solutions. When $a = 0.1$ mm, the relative error is 50.9% for M_p and 42.5% for V. The cause of the significant difference is that for smaller holes, the effects of the stress component σ_{zz} and the transverse shearing stress τ_{rz} near the hole on the deformation of the thin disk are ignored in the applied bending theory [20]. A future study has been planned to solve this problem. The hole radius is set as 1.5 mm in the following subsection to avoid the calculation deviations that occur in cases with smaller holes.

Furthermore, the signs for the peeling moments and shear forces in Fig. 7 merit attention. The changes in the peeling stresses along the interface from compressive at the hole edge to tensile in the in-board region give rise to closing modes of moments (i.e., $\hat{M}_p$ and M_p are positive), which may prevent mode I edge cracking. In addition, the signs of the shear stresses in Fig. 6 indicate the shear directions, and only their magnitudes are concerned for mode II edge cracking; thus $\hat{V}$ and V in Fig. 7 are written as positive to represent their magnitudes. Therefore, during the cooling period, the system is prone to mode II interfacial delamination from the hole edge promoted by interfacial shear stresses/forces. However, the situation may be different during the heating period. From Eqs. (A. 11) and (A. 13), $\hat{M}_p$ has linear relation with ΔT, which indicates that during the heating up period (ΔT is positive), $\hat{M}_p$ and M_p are negative (i.e. in opening modes) and mode I edge cracking will be promoted. In this case, mix-mode (including both modes I and II) edge cracking may occur near the hole of the system.

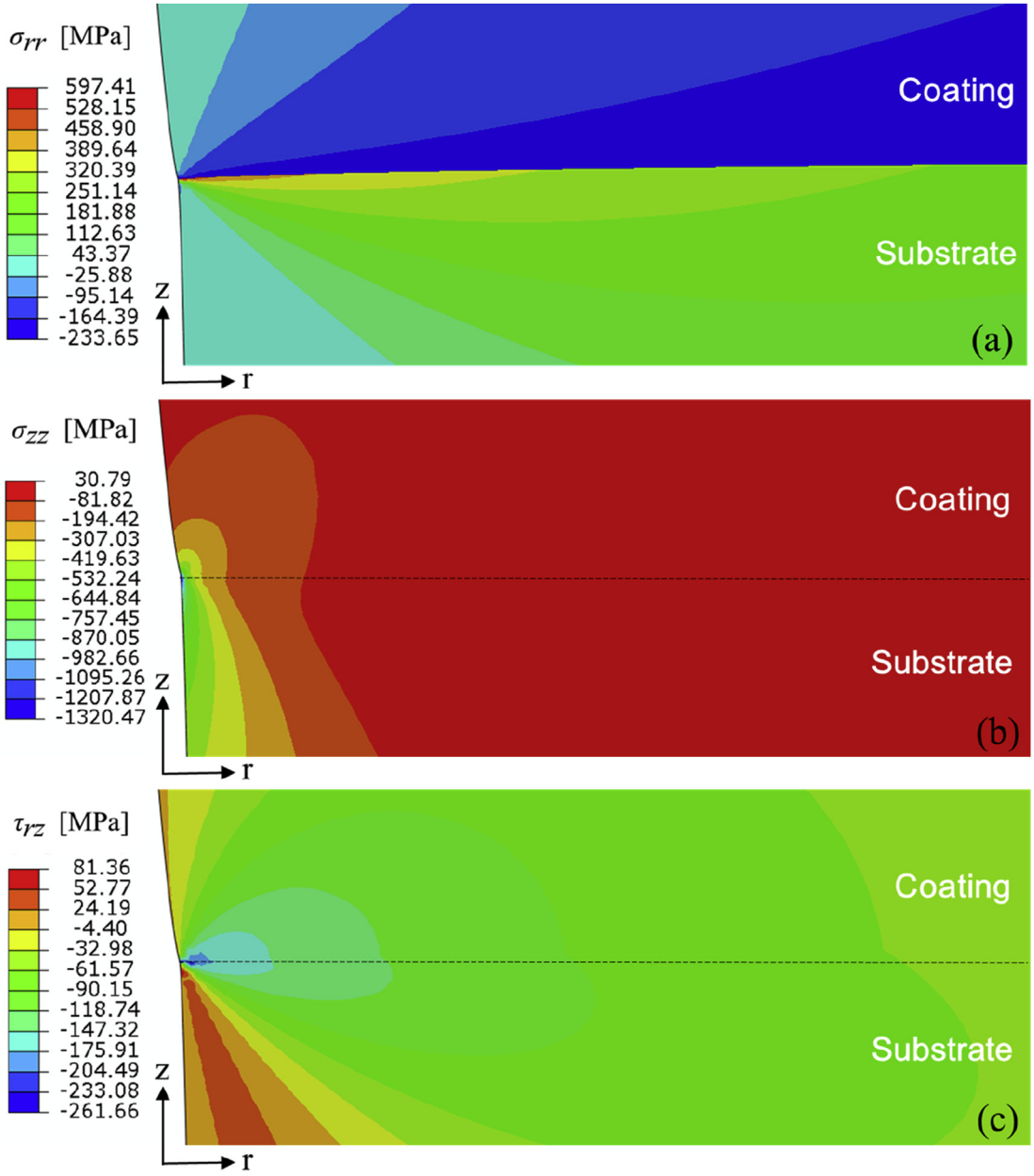

Fig. 5. FE results of the stress component distributions near the interface and hole edge in a double-layered model with a hole radius of 1.5 mm.

4.2. Four-layered system

The multilayered TBC system experiences more complicated stress distributions than the double-layered system. Fig. 8 shows the interfacial peeling and shear stresses along each interface of the four-layered TBC system with a hole radius of 1.5 mm. At each interface, σ_{zz} and τ_{rz} along the interface vary rapidly and significantly near the hole edge and then reach zero far from the hole edge. Generally, the shear stresses require a greater distance from the hole edge to reach zero than the peeling stresses. Near the hole edge, σ_{zz} and τ_{rz} each have their own variation trends from the hole edge at each interface. The σ_{zz} at the BC/substrate interface changes from a compressive state to a tensile state near the hole edge, like that in a double-layered system, whereas the σ_{zz} at the TC/TGO and TGO/BC interfaces change from tensile states to compressive states and then back to tensile states. The tensile stresses at the TC/TGO and TGO/BC interfaces near the hole edge appear only in very small regions, and it is unclear whether they promote model I edge cracking. The TGO/BC interface has a larger magnitude of τ_{rz} at the hole edge than the TC/TGO and BC/substrate interfaces, which may be more likely to cause mode II edge cracking.

Figs. 9 and 10 display the corresponding peeling moments and shear forces at three interfaces, and the respective effects of the TGO and TC thickness are considered. For all cases, the analytical solutions are in good agreement with the FE results. In Fig. 9, both M_p and V at the BC/substrate interface are larger than those at other interfaces. With TGO thickening, the M_p and V at the BC/substrate and TGO/BC interfaces increase, but they decrease slightly at the TC/TGO interface. The M_p is always positive (i.e., in closing mode) with TGO thickening, which may impede mode I edge cracks at all interfaces. As the TGO grows, mode II edge cracks is more likely to occur at both the BC/substrate and TGO/BC interfaces as a result of the increasing interfacial shear forces.

In Fig. 10, both M_p and V at the BC/substrate interface reach greater magnitudes than those at other interfaces as the TC thickness increases. At all interfaces, M_p and V increase as the TC thickness increases. Mode I edge cracking is impeded at all interfaces because the interfacial peeling moments are always positive (i.e., in closing mode), and mode

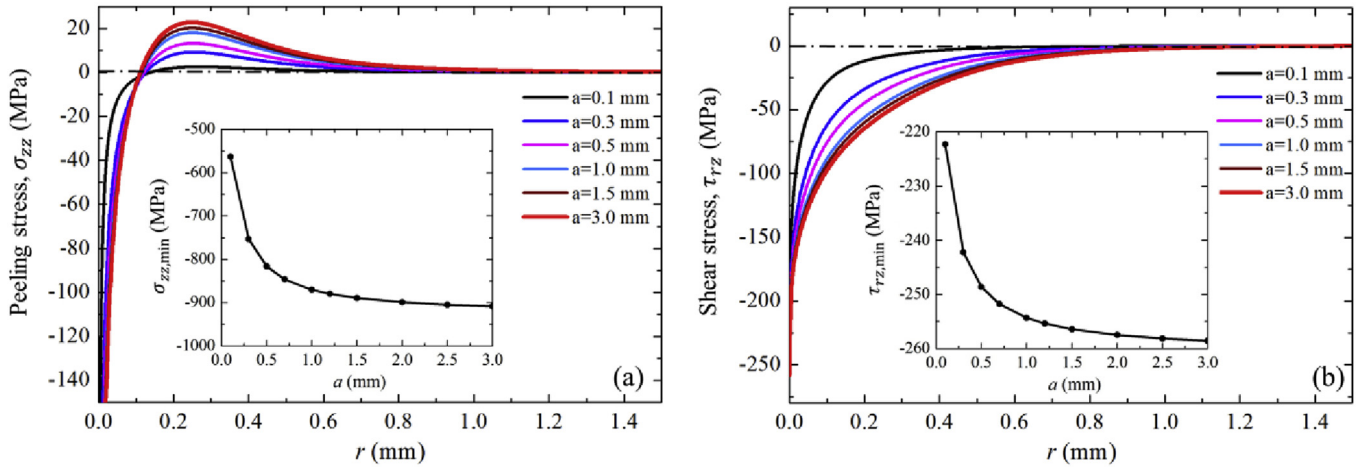

Fig. 6. FE results of the interfacial peeling stresses σ_{zz} and shear stresses τ_{rz} along the interface in a double-layered model with different hole radii. Note that r begins from the hole edge.

II edge cracking is promoted at all interfaces as a result of the increasing interfacial shear forces. Furthermore, based on Eqs. (10), (22) and (32), the interfacial peeling moment in each layer is negative (i.e., in opening modes) during the heating period (i.e., ΔT is positive), which could be the driving force for mode I edge cracking. In this case, mixed-mode edge delamination (including both modes I and II) may occur at the interfaces near the hole. Although a thicker TC leads to better thermal insulation properties, it also increases the risk of edge delamination in the TBC system near the cooling hole.

4.3. Interfacial cracking in TBCs at the hole edge

The above sections analyzed the stress distribution in TBCs around the hole, and M_p and V were chosen to predict the likelihood of the edge crack initiation from the hole. Now initiation and propagation of interfacial cracks from the hole edges during cooling-down periods modeled by CZM are presented. Fig. 11 and Fig. 12 display the patterns, lengths and initiation times of the interfacial cracks for different hole radii, a, when the TGO thickness is 5 μm. Note that SDEG in Fig. 11 represents the damage value in the interfacial cohesive elements

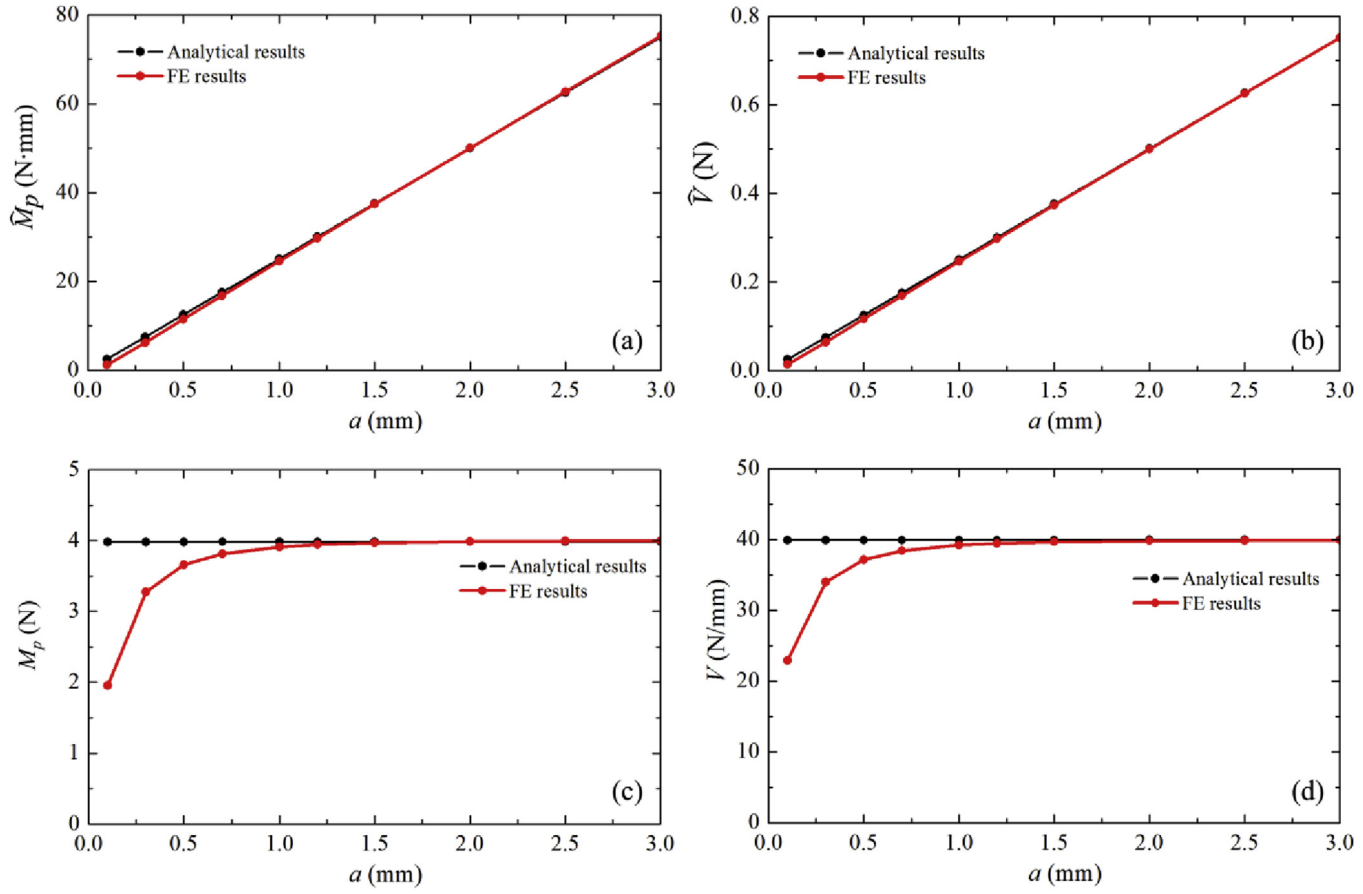

Fig. 7. Comparison of analytical and FE results of interfacial peeling moments and shear forces in a double-layered model with different hole radii.

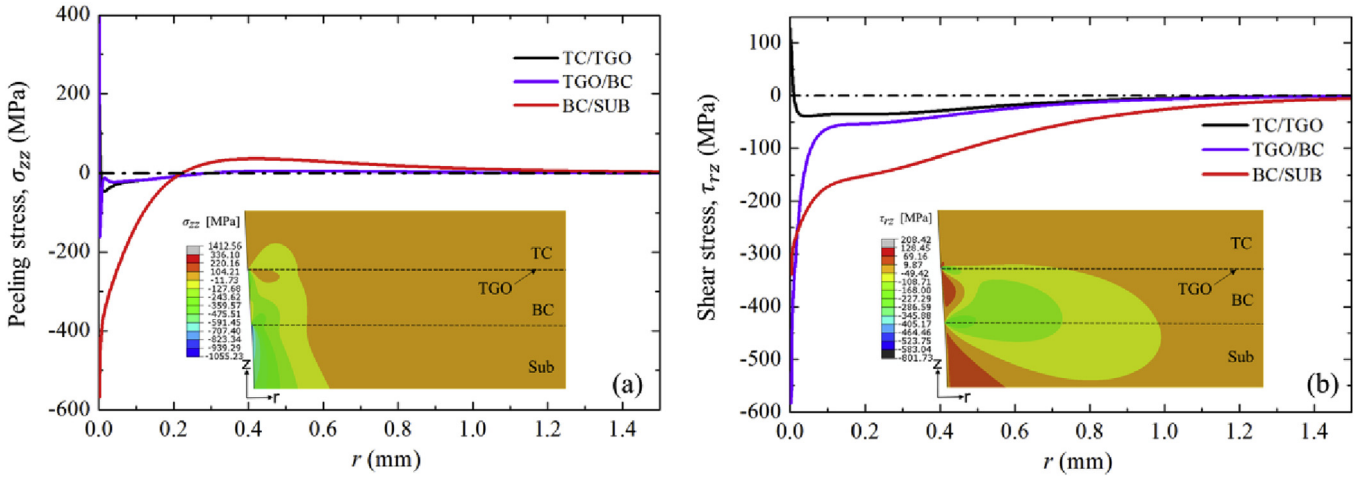

Fig. 8. FE results of the peeling stresses σ_{zz} and shear stresses τ_{rz} along different interfaces in a four-layered model. Note that r begins from the hole edge.

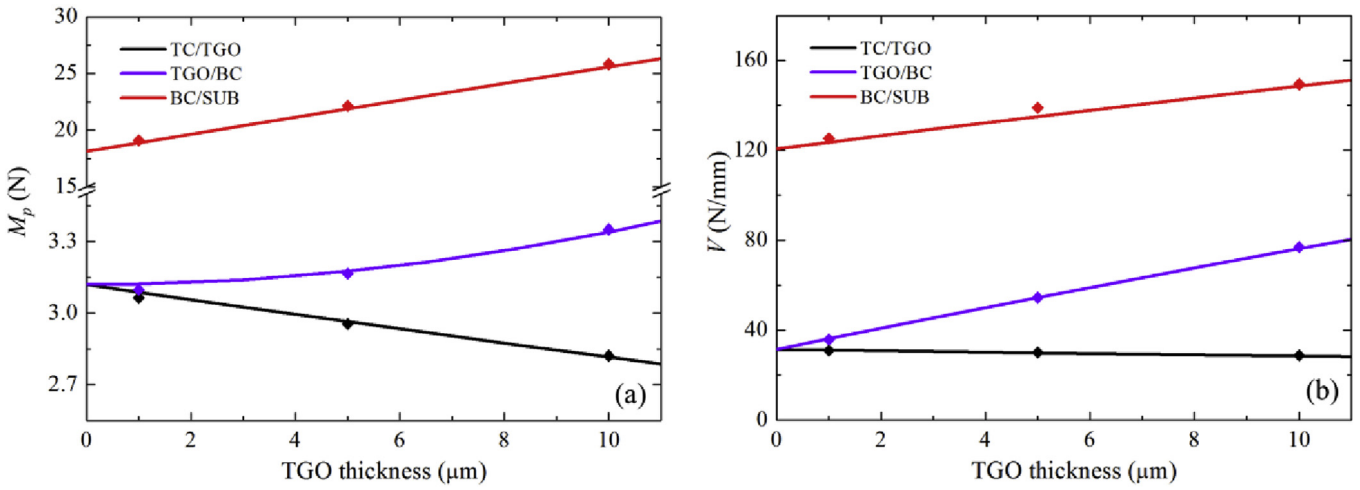

Fig. 9. Effect of TGO thickness on the interfacial peeling moments, M_p, and shear forces, V, at different interfaces in a four-layered model (lines: analytical solutions; symbols: FE results).

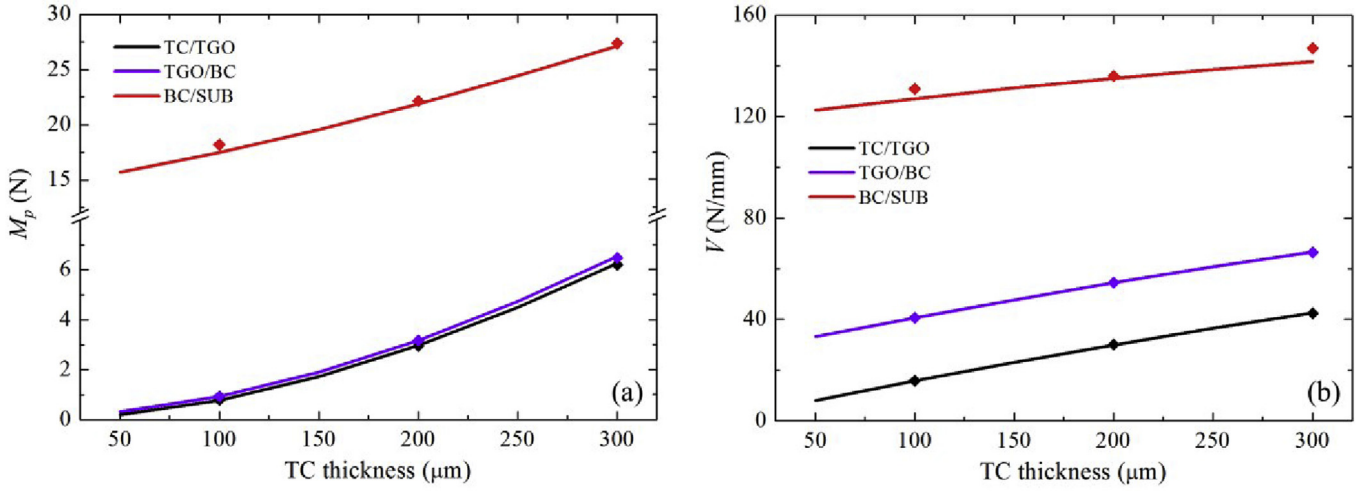

Fig. 10. Effect of TC thickness on the interfacial peeling moments, M_p, and shear forces, V, at different interfaces in a four-layered model (lines: analytical solutions; symbols: FE results).

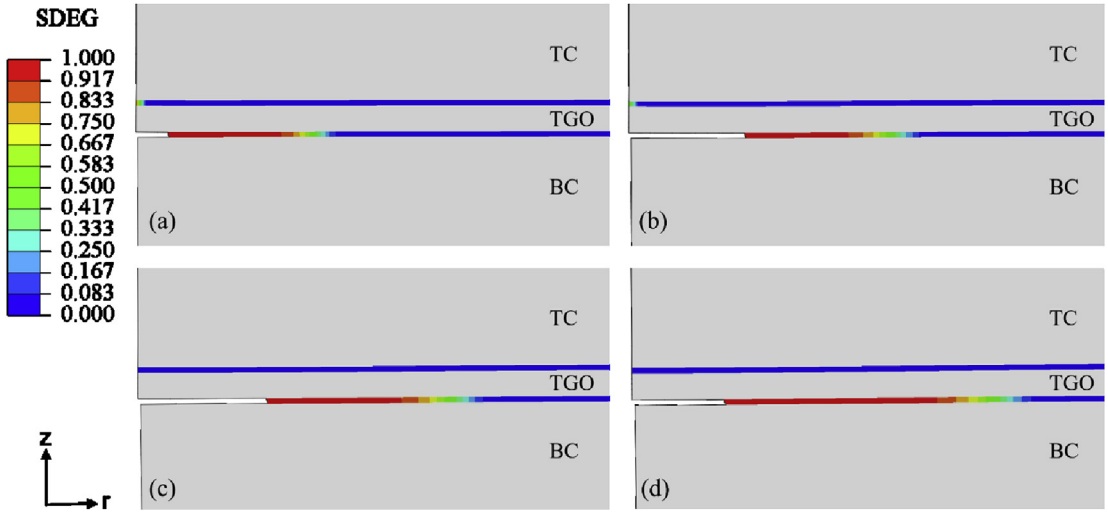

Fig. 11. Interfacial crack patterns near the hole for different hole radii, a, at room temperature when the TGO thickness is 5 μm: (a) a = 0.1 mm; (b) a = 0.25 mm; (c) a = 0.5 mm; (d) a = 1.0 mm. Note that SDEG represents the damage value ranging from 0 to 1. When SDEG = 0, there is no damage in the cohesive element; when SDEG = 1, failure occurs and the element is deleted to represent the crack surface.

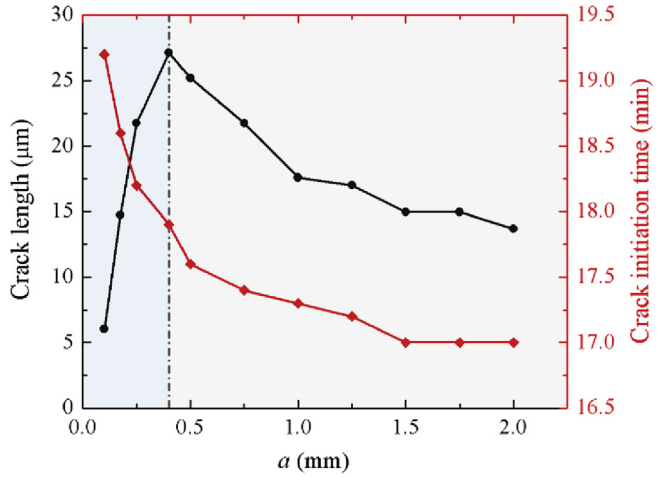

Fig. 12. Interfacial crack lengths and crack initiation times for different hole radii when the TGO thickness is 5 μm.

ranging from 0 to 1. When SDEG = 0, there is no damage in the cohesive element; when SDEG is accumulated to 1, failure occurs and the element is deleted to represent the crack surface. As shown in Fig. 11, edge cracks initiate and propagate only at the TGO/BC interface in all cases. This is because the shear stress at the TGO/BC interface at the hole edges is prominently larger than that at the TC/TGO interface, see Fig. 8b for instance, which makes the crack prone to initiate at the TGO/BC interface. Besides, once the crack occurs at the TGO/BC interface, the local stress near the TC/TGO interface will be relaxed to a low level, impeding the crack initiation at the TC/TGO interface.

In Fig. 12, as the hole radius becomes larger, the crack initiation time is shorter, namely the edge crack is more easily to initiate, which is consistent with the prediction by evaluating the magnitudes of M_p and V, see Fig. 7 for instance. However, the final crack length does not have a positive correlation with the hole radius. With the increase of hole radius, the crack length increases rapidly first and then decreases gradually to reach a certain value. The crack length reaches a maximum value of 27 μm when a = 0.4 mm. The results indicate that crack propagation cannot be accurately predicted by evaluating the stresses or M_p and V in models without considering damages. Once the interfacial crack appears, the stress field near the hole is redistributed, and the local stresses around the crack tip continuously prompt the crack propagation.

Fig. 13 shows the effect of both hole radius and TGO thickness on the interfacial crack length. When $a \leq 0.4$ mm, the interfacial crack is generated when the TGO layer is thick enough (> 3 μm), but when $a > 0.4$ mm, it can be generated with relatively thinner TGO layer (> 1 μm). For all cases, the interfacial crack propagates longer with TGO thickening. When the TGO thickness increases to 10 μm, the crack length for a = 0.5 mm reaches a maximum value of 69.2 μm. The results indicate that, under long-time thermal loadings, interfacial cracks in TBCs may initiate from the hole edge, and then propagate along the interface with the continuous TGO thickening. When the thermal loadings continue, the edge cracks may coalesce with the interfacial micro-cracks in regions remote from the hole to form a macro one, eventually resulting in local spallation of TBCs around the cooling hole.

5. Summary and remarks

The stress field and stress-induced interfacial cracking in TBCs near the cooling hole under uniform thermal loadings were investigated by analytical and numerical models. Analytical solutions for the interfacial peeling moment and shear force acting as the driving forces for mode I and mode II edge delamination were derived based on the mechanics of elasticity and the thin plate bending theory, and they were verified by the finite element calculations of the two- and four-layered coating-substrate systems with cooling holes. Furthermore, the interfacial cracks in TBCs initiated from the hole edges were simulated by the cohesive zone model. The results are as follows:

1) Because of the free-edge effect, both peeling and shear stresses at each interface are concentrated near the hole edge and then decay to negligible values in positions far from the hole. The TGO/BC interface in the four-layered system experiences the largest shear stresses at the hole edge, which is more likely to induce mode II edge cracking.
2) The interfacial peeling moment and shear force increase as the hole radius increases; however, for larger holes (i.e., hole radius greater than 1.5 mm), they can hardly increase and tend to remain constant. A TBC system with a larger cooling hole is more likely to initiate edge crack around the hole.
3) Upon cooling, the peeling moments in all layers are positive (i.e., in closing modes), which may impede mode I edge crack around the hole. Mode II edge crack is prone to be driven by the interfacial shear forces. However, upon heating, the peeling moments are

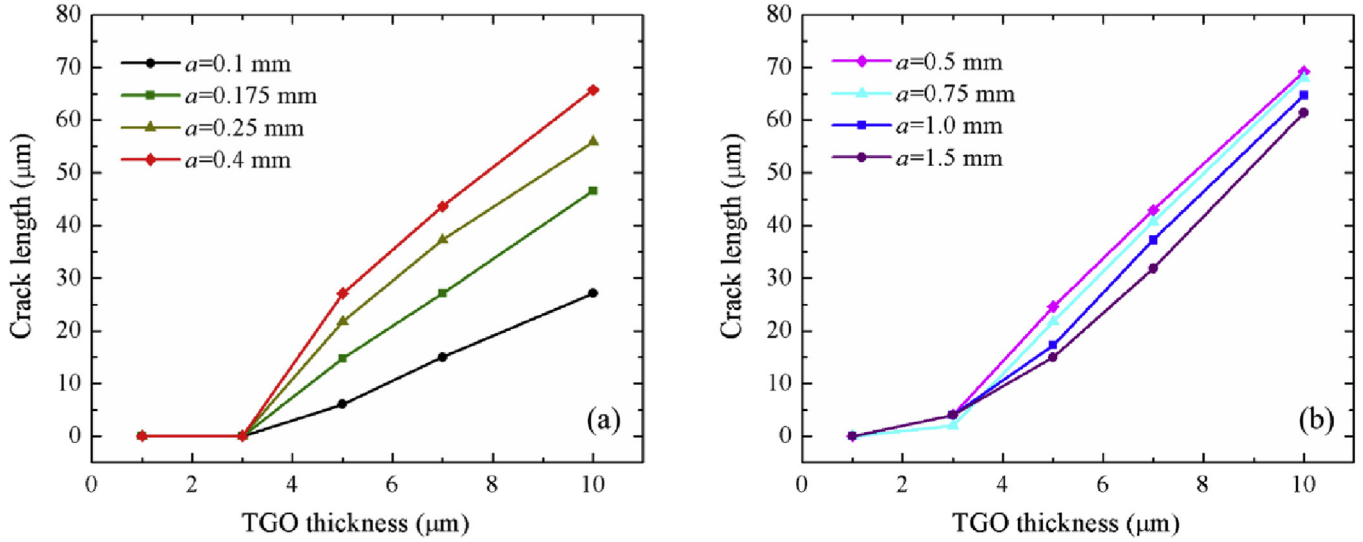

Fig. 13. Effect of hole radius and TGO thickness on the interfacial crack length.

negative (i.e., in opening modes). In this case, mixed-mode edge crack driven by both interfacial peeling moments and shear forces may occur at the interfaces near the hole.

4) Both the peeling moments and the shear forces increase at the TGO/BC and BC/substrate interfaces with TGO thickening, whereas they increase at all interfaces as the TC thickness increases. Greater TGO and TC thicknesses may increase the likelihood of interfacial mode II edge crack around the hole during the cooling period.
5) Derived by local stresses, interfacial crack between the TGO and BC initiates from the hole edge and then propagates along the interface during the cooling-down period. With the increase of hole radius, the crack length increases rapidly first and then decreases gradually to reach a certain value. The crack length reaches a maximum value of 27 μm when the hole radius is 0.4 mm for TBCs with TGO thickness of 5 μm. Furthermore, the edge crack propagates longer with TGO thickening, eventually resulting in local spallation of TBCs around the cooling hole.

Acknowledgements

This project is supported by China Postdoctoral Science Foundation (2019M653173 and 2019TQ0374), Guangdong Education Department Fund (2016KQNCX005) and Guangdong Provincial key S&T Special Project (2017B020235001 and 2019B010943001) and National Natural Science Foundation of China (No. 11902370).

Appendix A. Detailed analytical solutions for a double-layered system

The solutions for a double-layered system can be derived from the solutions presented in Sections 2.2 and 2.3 by letting the number of coating layer n = 1. Thus, the parameters c, t_b, and c_1 are calculated by

$$c = \frac{\frac{E_s h_s \alpha_s \Delta T}{1-\nu_s} + \frac{E_1 h_1 \alpha_1 \Delta T}{1-\nu_1}}{\frac{E_s h_s}{1-\nu_s} + \frac{E_1 h_1}{1-\nu_1}} \tag{A. 1}$$

$$t_b = \frac{\frac{-E_s h_s^2}{1-\nu_s}\left(1 + \frac{1-\nu_s}{1+\nu_s}\frac{b^2}{r^2}\right) + \frac{E_1 h_1^2}{1-\nu_1}\left(1 + \frac{1-\nu_1}{1+\nu_1}\frac{b^2}{r^2}\right)}{\frac{2E_s h_s}{1-\nu_s}\left(1 + \frac{1-\nu_s}{1+\nu_s}\frac{b^2}{r^2}\right) + \frac{2E_1 h_1}{1-\nu_1}\left(1 + \frac{1-\nu_1}{1+\nu_1}\frac{b^2}{r^2}\right)} \tag{A. 2}$$

$$c_1 = \frac{-\frac{E_s h_s (c-\alpha_s \Delta T)}{1-\nu_s}\left(\frac{h_s}{2} + t_b^{r=a}\right) + \frac{E_1 h_1 (c-\alpha_1 \Delta T)}{1-\nu_1}\left(\frac{h_1}{2} - t_b^{r=a}\right)}{\frac{2E_s h_s^2}{1-\nu_s}\left(\frac{h_s}{3} + \frac{t_b^{r=a}}{2}\right)\left(1 + \frac{1-\nu_s}{1+\nu_s}\frac{b^2}{a^2}\right) + \frac{2E_1 h_1^2}{1-\nu_1}\left(\frac{h_1}{3} - \frac{t_b^{r=a}}{2}\right)\left(1 + \frac{1-\nu_1}{1+\nu_1}\frac{b^2}{a^2}\right)} \tag{A. 3}$$

When $b \gg a$, $\frac{b^2}{a^2} \to +\infty$, then t_b for $r = a$ is calculated by

$$t_{b,r=a} \cong = \frac{-\frac{E_s h_s^2}{1+\nu_s} + \frac{E_1 h_1^2}{1+\nu_1}}{\frac{2E_s h_s}{1+\nu_s} + \frac{2E_1 h_1}{1+\nu_1}} \tag{A. 4}$$

The deflection w can then be calculated by substituting Eq. (A. 3) into Eq. (23). The curvature, $\frac{1}{\rho}$, is expressed as

$$\frac{1}{\rho} = -\frac{d^2 w}{dr^2} = -2c_1\left(1 + \frac{b^2}{r^2}\right) \tag{A. 5}$$

Considering $b \gg a$, $\frac{1}{\rho}$ for $r = a$ is calculated by

$$\left(\frac{1}{\rho}\right)_{r=a} \cong \frac{\frac{E_s h_s(c-\alpha_s\Delta T)}{1-\nu_s}\left(\frac{h_s}{2}+t_b^{r=a}\right)-\frac{E_1 h_1(c-\alpha_1\Delta T)}{1-\nu_1}\left(\frac{h_1}{2}-t_b^{r=a}\right)}{\frac{E_s h_s^2}{1+\nu_s}\left(\frac{h_s}{3}+\frac{t_b^{r=a}}{2}\right)+\frac{E_1 h_1^2}{1+\nu_1}\left(\frac{h_1}{3}-\frac{t_b^{r=a}}{2}\right)} \tag{A. 6}$$

and for $r = b$,

$$\left(\frac{1}{\rho}\right)_{r=b} = 0 \tag{A. 7}$$

The in-plane stresses σ_{rr}^s for substrate and σ_{rr}^1 for coating (i.e., TC) in regions remote from the hole edges are calculated as

$$\sigma_{rr}^s = -2E_s\left[\frac{1}{1-\nu_s}+\frac{b^2}{(1+\nu_s)r^2}\right](z-t_b)c_1+\frac{E_s c-E_s\alpha_s\Delta T}{1-\nu_s} \tag{A. 8a}$$

$$\sigma_{rr}^1 = -2E_1\left[\frac{1}{1-\nu_1}+\frac{b^2}{(1+\nu_1)r^2}\right](z-t_b)c_1+\frac{E_1 c-E_1\alpha_1\Delta T}{1-\nu_1} \tag{A. 8b}$$

From Eqs. (A. 8a) and (A. 8b), σ_{rr}^s and σ_{rr}^1 are functions of r and z. The interfacial peeling moment M_p and the shear force V are calculated by, respectively,

$$M_p = \frac{E_1 h_1^2 c_1}{1-\nu_1}\left(\frac{2h_1}{3}-t_b^{r=a}\right)\left(1+\frac{1-\nu_1}{1+\nu_1}\frac{b^2}{a^2}\right)-\frac{E_1 h_1^2(c-\alpha_1\Delta T)}{2(1-\nu_1)} \tag{A. 9}$$

$$V = \frac{E_1 h_1 c_1}{1-\nu_1}(h_1-2t_b^{r=a})\left(1+\frac{1-\nu_1}{1+\nu_1}\frac{b^2}{a^2}\right)-\frac{E_1 h_1(c-\alpha_1\Delta T)}{1-\nu_1} \tag{A. 10}$$

Considering $b \gg a$ and substituting Eq. (A. 3) into Eqs. (A. 9) and (A. 10), M_p and V can be simplified as

$$M_p = \frac{E_1 h_1^2 P}{1-\nu_1}\left(\frac{2h_1}{3}-t_b^{r=a}\right)-\frac{E_1 h_1^2(c-\alpha_1\Delta T)}{2(1-\nu_1)} \tag{A. 11}$$

$$V = \frac{E_1 h_1 P}{1-\nu_1}(h_1-2t_b^{r=a})-\frac{E_1 h_1(c-\alpha_1\Delta T)}{1-\nu_1} \tag{A. 12}$$

where

$$P \cong \frac{\frac{E_s h_s(c-\alpha_s\Delta T)}{1-\nu_s}\left(\frac{h_s}{2}+t_b^{r=a}\right)-\frac{E_1 h_1(c-\alpha_1\Delta T)}{1-\nu_1}\left(\frac{h_1}{2}-t_b^{r=a}\right)}{\frac{-2E_s h_s^2}{1-\nu_s}\left(\frac{h_s}{3}+\frac{t_b^{r=a}}{2}\right)\left(\frac{1-\nu_s}{1+\nu_s}\right)\left(\frac{1+\nu_1}{1-\nu_1}\right)+\frac{-2E_1 h_1^2}{1-\nu_1}\left(\frac{h_1}{3}-\frac{t_b^{r=a}}{2}\right)} \tag{A. 13}$$

From Eqs. (A. 11)-(A. 13), M_p and V are independent of a and b. In other words, by the presented analytical solutions, the interfacial peeling moment M_p and the shear force V remain unchanged regardless of the size of the cooling hole.

References

[1] N.P. Padture, M. Gell, E.H. Jordan, Thermal barrier coatings for gas-turbine engine applications, Science 296 (5566) (2002) 280–284.
[2] D.R. Clarke, M. Oechsner, N.P. Padture, Thermal-barrier coatings for more efficient gas-turbine engines, MRS Bull. 37 (10) (2012) 891–898.
[3] K.M. Kim, S. Shin, H.L. Dong, H.H. Cho, Influence of material properties on temperature and thermal stress of thermal barrier coating near a normal cooling hole, Int. J. Heat Mass Transf. 54 (25–26) (2011) 5192–5199.
[4] J.S. Jiang, L.X. Jiang, Z.W. Cai, W.Z. Wang, X.F. Zhao, Y.Z. Liu, Z.M. Cao, Numerical stress analysis of the TBC-film cooling system under operating conditions considering the effects of thermal gradient and TGO growth, Surf. Coat. Technol. 357 (2019) 433–444.
[5] N. Sundaram, K.A. Thole, Effects of surface deposition, hole blockage, and TBC spallation on vane endwall film-cooling, ASME Turbo Expo 2006: Power Land Sea Air 129 (2006) 599–607.
[6] E. Sun, T. Heffernan, R. Helmink, Stress Rupture and Fatigue in Thin-Wall Single-Crystal Superalloys with Cooling Holes, John Wiley & Sons, Inc., Hoboken, NJ, 2012.
[7] F.X. Li, K.J. Kang, Deformation and cracking near a hole in an oxide-forming alloy foil subjected to thermal cycling, Acta Mater. 61 (1) (2013) 385–398.
[8] X. Peng, N. Sridhar, D.R. Clarke, The stress distribution around goles in thermal barrier coatings, Mater. Sci. Eng. A 380 (1) (2004) 208–214.
[9] A.G. Evans, D.R. Mumm, J.W. Hutchinson, G.H. Meier, F.S. Pettit, Mechanisms controlling the durability of thermal barrier coatings, Prog. Mater. Sci. 46 (5) (2001) 505–553.
[10] C.H. Hsueh, Thermal stresses in elastic multilayer systems, Thin Solid Films 418 (2) (2002) 182–188.
[11] X.C. Zhang, B.S. Xu, H.D. Wang, Y.X. Wu, An analytical model for predicting thermal residual stresses in multilayer coating systems, Thin Solid Films 488 (1) (2005) 274–282.
[12] H.H. Yu, M.Y. He, J.W. Hutchinson, Edge effects in thin film delamination, Acta Mater. 49 (1) (2001) 93–107.
[13] E. Suhir, Stresses in BiMetal thermostats, J. Appl. Mech.T ASME 56 (3) (1989) 595–600.
[14] J.W. Eischen, C. Chung, J.H. Kim, Realistic modeling of edge effect stresses in bi-material elements, ASME. J. Electron. Packag. 112 (1) (1990) 16–23.
[15] Y.H. Pao, E. Eisele, Interfacial shear and peel stresses in multilayered thin stacks subjected to uniform thermal loading, ASME. J. Electron. Packag. 113 (2) (1991) 164–172.
[16] T. Kant, K. Swaminathan, Estimation of transverse/interlaminar stresses in laminated composites–a selective review and survey of current developments, Compos. Struct. 49 (1) (2000) 65–75.
[17] T.D. Moore, Thermomechanical peeling in multilayer beams and plates—a solution from first principles, Int. J. Solids Struct. 42 (1) (2005) 271–285.
[18] C.H. Hsueh, C.R. Luttrell, S. Lee, T.C. Wu, H.Y. Lin, Interfacial peeling moments and shear forces at free edges of multilayers subjected to thermal stresses, J. Am. Ceram. Soc. 89 (5) (2006) 1632–1638.
[19] C.H. Hsueh, A.G. Evans, Residual stresses in meta/ceramic bonded strips, J. Am. Ceram. Soc. 68 (5) (1985) 241–248.
[20] S.P. Timoshenko, K. Woinowsky-Krieger, Theory of Plates and Shells, Mc-Graw-Hill, New York, 1959.
[21] L. Chen, G.J. Yang, C.X. Li, C.J. Li, Edge effect on crack patterns in thermally sprayed ceramic splats, J. Therm. Spray Technol. 26 (3) (2017) 302–314.
[22] J.S. Jiang, W.Z. Wang, X.F. Zhao, Y.Z. Liu, Z.M. Cao, P. Xiao, Numerical analyses of the residual stress and top coat cracking behavior in thermal barrier coatings under cyclic thermal loading, Eng. Fract. Mech. 196 (2018) 191–205.
[23] Version ABAQUS. 6.13, Analysis User's Guide, Dassault Systems, 2013.
[24] C. Chung, J.W. Eischen, The free-edge stress singularity at an interface between bilinear materials, Int. J. Solids Struct. 28 (1) (1991) 105–113.